processes

MDPI

Article

Modeling and Optimization of the Vacuum Degassing Process in Electric Steelmaking Route

Bikram Konar [1,*], Noah Quintana [2] and Mukesh Sharma [1]

[1] EVRAZ North America, Research and Development, 100 Armor Road, Regina, SK S4K 0A8, Canada; mukesh.sharma@evrazna.com
[2] EVRAZ North America, Rocky Mountain Steel, 2100 South Freeway, Pueblo, CO 81004, USA
* Correspondence: bikram.konar@evrazna.com; Tel.: +1-(306)-924-7456

Abstract

Vacuum degassing (VD) is a critical refining step in electric arc furnace (EAF) steelmaking for producing clean steel with reduced nitrogen and hydrogen content. This study develops an Effective Equilibrium Reaction Zone (EERZ) model focused on denitrogenation (de-N) by simulating interfacial reactions at the bubble–steel interface (Z1). The model incorporates key process parameters such as argon flow rate, vacuum pressure, and initial nitrogen and sulfur concentrations. A robust empirical correlation was established between de-N efficiency and the mass of Z1, reducing prediction time from a day to under a minute. Additionally, the model was further improved by incorporating a dynamic surface exposure zone (Z_eye) to account for transient ladle eye effects on nitrogen removal under deep vacuum (<10 torr), validated using synchronized plant trials and Python-based video analysis. The integrated approach—combining thermodynamic-kinetic modeling, plant validation, and image-based diagnostics—provides a robust framework for optimizing VD control and enhancing nitrogen removal control in EAF-based steelmaking.

Keywords: vacuum tank degasser; EERZ; slag eye; exposure metric; nitrogen removal

Academic Editors: Yuanqiang Zhou, Le Yao, Xiaoyu Jiang and Zheren Zhu

Received: 12 June 2025
Revised: 8 July 2025
Accepted: 15 July 2025
Published: 25 July 2025

Citation: Konar, B.; Quintana, N.; Sharma, M. Modeling and Optimization of the Vacuum Degassing Process in Electric Steelmaking Route. *Processes* **2025**, *13*, 2368. https://doi.org/10.3390/pr13082368

1. Introduction

Vacuum degassing (VD) plays a pivotal role in modern Electric Arc Furnace (EAF)-based steelmaking operations, enhancing the quality and purity of molten steel by addressing the removal of undesirable gaseous elements (predominantly nitrogen [N] and hydrogen [H]). VD contributes to denitrogenation [1–5], dehydrogenation [4,6], desulfurization [4,5,7], decarburization [4,5], and inclusion removal [8,9]. Excess nitrogen combines with aluminum or microalloying elements like V, Nb, or Ti and reduces hot ductility and promotes transverse cracking during casting due to nitride or carbonitride precipitation [10]. High nitrogen also lowers the ductile-to-brittle transition temperature and increases fracture risk. In Ti-containing steels, a Ti/N ratio $\geq$ 2.9 enhances boron hardenability, but high (Ti)(N) products lead to coarse TiN formation and reduced toughness after heat treatment [11,12]. The primary objective of VD is to achieve the required amount of N and H in steel, leading to improved consistency in mechanical properties and better reliability in downstream thermo-mechanical processing.

Nitrogen removal during VD occurs via (i) argon bubble absorption, (ii) surface degassing through the open-eye region, and (iii) spontaneous bubble nucleation [13], all of which depend on the argon injection through a porous plug in the ladle and the vacuum pressure achieved in the degassing tank. Although VD typically operates under fixed

argon flow and vacuum profiles, fluctuations in incoming steel composition, especially nitrogen, sulfur, and oxygen, can affect nitrogen removal efficiency and necessitate dynamic process adjustments. Visual monitoring of the ladle eye, commonly used to assess flow and exposure, is limited by poor visibility and infrequent sampling, especially during initial stirring. To overcome these limitations, indirect sensing techniques have been explored. Laboratory-scale liquid metal and water model experiments [14–16] using accelerometers and wavelet-based vibration signal analysis have shown promise in capturing bubble behavior and flow regimes. Industrial validation [14,15,17–19] further demonstrated the correlation between vibrational signatures, such as the Ladle Resonance Value (LRV) and gas removal efficiency. However, these methods cannot resolve spatial or temporal variations in gas–metal interfacial interactions.

Alongside experiments, several modeling studies have attempted to characterize nitrogen removal kinetics in VD [20–22]. Traditional models often consider mass transfer from bulk steel to the gas–metal interface, followed by surface chemical reactions and gas-phase desorption [3,23]. The rate-limiting step varies with process conditions: chemical reactions dominate when surface-active elements like oxygen or sulfur are abundant, while mass transfer becomes rate-controlling at low concentrations [3,24,25].

Recent advancements in computational fluid dynamics (CFD), typically using Euler–Euler formulations, have enabled more detailed treatment of stirring and interfacial dynamics. These models, though offering improved fidelity in fluid dynamics, rely on limited thermodynamic data to estimate nitrogen activity coefficients based on steel composition and temperature [2,26], which constrains their predictive accuracy and contributes to their computational intensity for real-time plant applications.

Recognizing the limitations of both indirect sensing and traditional models in capturing the dynamic, multi-component nature of vacuum degassing, this study introduces a novel nitrogen removal model based on the Effective Equilibrium Reaction Zone (EERZ) approach [27,28]. The EERZ framework divides complex metallurgical reactions into discrete thermodynamically equilibrated zones with defined homogenization timescales, allowing kinetic effects to be embedded through tunable zone volumes and mixing frequencies reflective of gas stirring, phase interactions, and chemical affinities.

A key innovation is the inclusion of the Zone at Eye (*Z_eye*)—representing the vacuum-exposed open-eye region—as a dynamic contributor to nitrogen removal. This feature, often absent in traditional models, is quantified using a custom Python-based video analysis tool applied to real-time plant operational video during VD. The tool extracts ladle eye exposure metrics in real time, enabling precise alignment between observed behavior and model predictions.

By integrating thermodynamics, empirical kinetics, zone-based modeling, and plant-derived visual data, the proposed VD model captures transient steel–bubble–vacuum–slag interactions more effectively. This hybrid methodology enhances predictive accuracy while remaining computationally lightweight, offering a practical and robust framework for optimizing nitrogen control during vacuum degassing in the electric steelmaking route.

2. Process Description, Argon Stirring, and Operational Data Acquisition in Vacuum Degassing

2.1. Process Description and Argon Stirring Phenomena

In secondary steelmaking, vacuum treatment reduces the ambient pressure around the molten steel, lowering the solubility of dissolved gases and promoting their removal. Argon (Ar) injection plays a vital role by inducing stirring, which accelerates mass transfer and aids the escape of gases from the steel to the vacuum environment. The effectiveness of this process depends on factors such as vacuum pressure, Ar flow rate, treatment duration

(typically ~30 min), and the concentrations of dissolved elements, which influence the gas–metal reaction equilibria.

A characteristic feature of Ar stirring is the formation of a slag eye (*Z_eye*)—a localized region where the slag layer is displaced by the gas plume, exposing the molten steel to vacuum. This phenomenon significantly affects degassing by enhancing gas–metal–slag interactions.

The characteristics of slag eye formation have been extensively studied using physical water models, which provide valuable insights into the hydrodynamic effects of gas stirring on slag behavior. Krishnapisharody and Irons [29,30] observed that slag viscosity has minimal impact at low gas flow rates; however, at higher flow rates, more viscous slags slightly increased eye size. Their experiments with thick oil layers simulating slag showed negligible eye size variation across different flow conditions. Iguchi et al. [31] reported that thick slags combined with low gas flow promote a recirculating flow pattern, whereas thin slags under high flow allow plume breakthrough, resulting in spout or plume eyes. Amaro-Villeda et al. [32] demonstrated that eye size increases with decreasing viscosity, regardless of slag thickness. Similarly, in water modeling studies, Peranandhanthan and Mazumdar [33] observed a direct relationship between slag kinematic viscosity and eye size. However, other researchers, including Wu et al. [34] and Ramasetti et al. [35], reported minimal effects from viscosity and interfacial tension. Conejo and Feng [36] synthesized findings across multiple studies and suggested an inverse relationship between slag viscosity and eye size. Despite these differing conclusions, the literature generally indicates that slag density and kinematic viscosity significantly influence slag eye behavior during ladle gas stirring, while interfacial tension does not have any effect on slag eye size.

In this study, the plume and slag eye area models from Krishnapisharody and Irons [29,30] are used to evaluate the influence of operational parameters on Z_eye formation. Although slag viscosity remained relatively constant across heats (refers to a batch of steel contained in the ladle after EAF) of the same grade, slag thickness and density were analyzed as key variables affecting eye behavior and gas–liquid interactions. These factors play a central role in understanding how Ar stirring disrupts the slag layer and enhances the overall degassing process.

2.2. Plant Operation and Vacuum Degassing Configuration

The steelmaking operation is primarily scrap-based, which produces steel using an EAF, which is tapped and refined at the Ladle Furnace (LF), followed by Vacuum Tank Degasser (VTD), and subsequently cast into rounds with diameters ranging from 7.5 to 12.25 inches in a six-strand continuous caster. The VTD utilizes a single porous plug for Ar injection. During VD, the automation system records the amount of Ar injection rate (in SCFM), vessel pressure (in torr), and the VTD is equipped with an air-cooled high-definition camera and vibration sensors.

Figure 1 illustrates a schematic of an ideal VD processing, where the ambient pressure is decreased, and the Ar gas injection rate is increased to their respective minimum and maximum values during the deep-vacuum stage. As the VD process enters this stage, the slag eye becomes visible. Video feed from the camera and data from vibration sensors are continuously recorded throughout the VD process.

In this work, the observed slag eye (ladle eye) images are discussed in the following section and have been used as a key tool to constrain one of the parameters of the EERZ model. While online off-gas monitoring could have provided a more holistic understanding of the process thermodynamics and kinetics, it was not conducted during the heats discussed in this study. Both slag/steel samples were acquired at tstart and tfinish at atmospheric pressure (1 atm, without vacuum). The difference between t_{start} and t_{finish} can

be considered as the actual time (secs). Utilizing online feedback and steel/slag sampling with off-gas monitoring is sufficient to derive a computational model of the VD process and predict its kinetics.

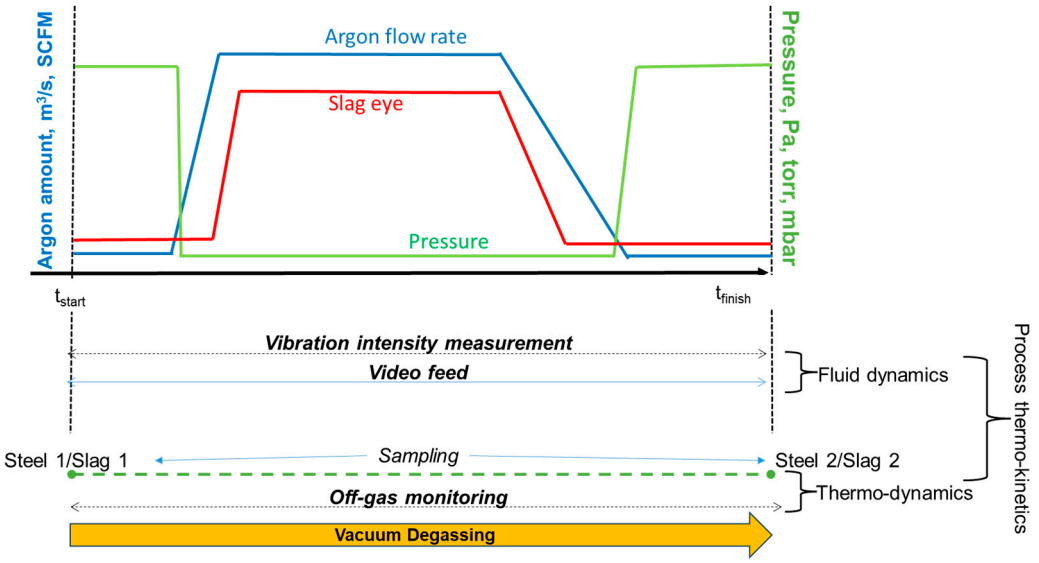

Figure 1. Schematic of a typical VD process, including primary process parameters, real-time process data, and materials during the operation. The sampling refers to the incoming and outgoing steel/slag samples, which is derived at the start and finish points of VTD. Continuous off-gas monitoring also enables us to understand the process thermo-kinetics.

2.3. Real-Time Data Acquisition and Slag Eye Visualization

The VTD automation records real-time measurements of Ar flow rate and pressure at the porous plug, along with the vessel pressure (ambient atmosphere to which the ladle is exposed). During the degassing process, an air-cooled, high-definition camera captures the top surface of the ladle, recording the slag cover and the steel-eye/spout when exposed to the atmosphere. The video recorded by the camera can be correlated with other real-time process parameters.

Figure 2 illustrates a typical VD processing sequence, showcasing recorded ambient atmosphere pressure, Ar gas injection rates, and snapshots from a standard video camera feed at specific instances during the processing time. The observations made at these instances are as follows:

(a) ~300 s: The vessel pressure is sufficiently low (<0.1 bar), and the ladle eye starts becoming visible. However, at this point, the ladle eye is still unstable (wobbly) and may close and re-open. The lower vessel pressure aids in reducing dust, ultimately improving the clarity of the video feed.

(b) ~550 s: VD enters the deep-vacuum stage (<0.01 bar), leading to the stabilization of the ladle eye.

(c) ~650 s: VD continues in the deep-vacuum stage, and with the increase in the Ar injection rate, the ladle eye size experiences a significant increase.

(d) ~800 s: VD, with the maximum Ar injection rate and low vessel pressure (deep vacuum), results in a significantly turbulent ladle eye with bubbly steel and occasional splashes. The ladle eye size extends to almost 80% of the ladle diameter, and there is notable mixing between hot steel and slag layers.

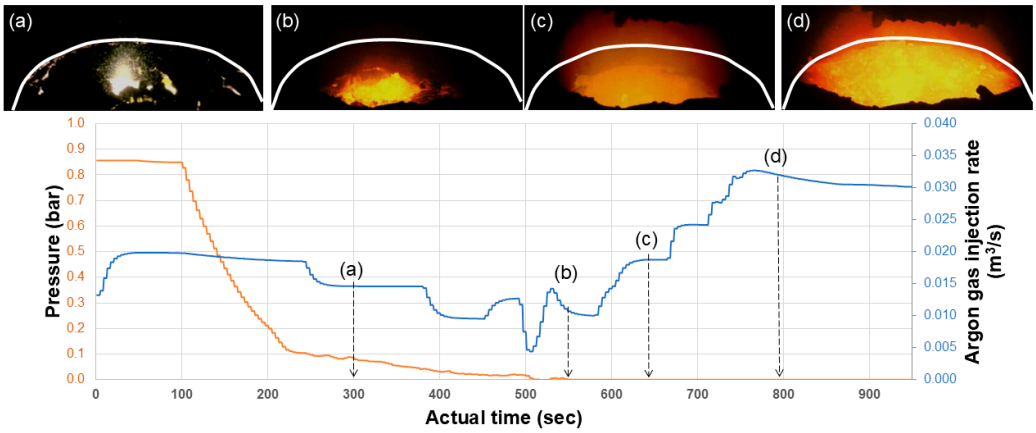

Figure 2. Snapshots from the video recording at different processing instances: (**a**) 300 s, (**b**) 550 s, (**c**) 650 s, and (**d**) 800 s, along with the vessel pressure and Ar injection rate.

The video stream is continuously monitored online to verify the performance of the Ar-plug. In the present work, the video and time-specific snapshot data have been further analyzed, incorporating image processing techniques for measuring the ladle eye size. Based on these phenomenological observations, the VD process model is constructed and tuned to VD processing time (s): [actual time—250] s.

2.4. Sampling and Compositional Analysis of Steel and Slag

The chemical compositions of VTD slag and steel samples are analyzed as follows:

a. Steel samples: Elemental composition is measured using an Optical Emission Spectrometer (OES, ARL Model 4460) manufactured by Thermo Fisher Scientific, Écublens, Vaud, Switzerland. Steel lollipops extracted from the heats are used for this analysis.
b. Slag samples: Elemental constituents are determined using an X-Ray Fluorescence analyzer (XRF, Bruker S8 Tiger) manufactured by Bruker AXS GmbH, Karlsruhe, Germany. The XRF analysis involves a finely ground powder of the slag sample and identifies slag components based on internal calibration.

In this study, three heats were employed to model and validate the VD process using the EERZ approach. Tables 1 and 2 present summaries of the steel and slag chemistries of the three heats before the VD process. The steel chemistry measurements before and after the VD process were crucial for modeling and interpreting the results within the EERZ framework. In the current iteration of the VD process model, slag chemistry data were primarily used in density calculation equations to determine the ladle eye size.

Table 1. Steel chemistry entering the Vacuum Tank Degasser (scrap-based EAF).

Heats	Fe, wt. %	C, wt. %	Mn, wt. %	Si, wt. %	S, ppm	N, ppm
1	~98.5	0.76	0.76	0.245	130	93
2	~98.5	0.55	0.71	0.265	130	77
3	~98.5	0.22	0.60	0.200	120	62

Table 2. Slag chemistry (normalized) entering the Vacuum Tank Degasser.

Heats	CaO, wt. %	Al_2O_3, wt. %	SiO_2, wt. %	MgO, wt. %	FeO, wt. %	MnO, wt. %
1	49.1	7.0	33.0	9.7	0.9	0.3
2	47.8	5.0	31.9	13.4	1.4	0.6
3	53.9	3.2	29.7	12.0	1.0	0.2

2.5. Plant Data Verification

The following plant data were utilized for the development and verification of the model:

a. Nitrogen content in the steel before and after degassing.
b. Rate of nitrogen removal, calculated as the nitrogen content drop per unit time, based on the total duration of the VD process.
c. Exposure metric, derived from video footage of the ladle open-eye region, capturing the extent of steel surface exposure and ladle-eye dimensions.
d. Stirring metric, obtained through vibration analysis using a tri-axial accelerometer mounted on the exterior of the VD tank. The accelerometer recorded data at a sampling frequency of up to 500 Hz.

3. Modeling Implementation and Workflow

3.1. Effective Equilibrium Reaction Zone (EERZ) Modeling

The EERZ model has been employed to model the VD process. Recently, various steelmaking processes [27,28] have been successfully modeled using the EERZ framework, leveraging FactSage [37] thermodynamic databases. EERZ modeling enables the decoupling of complex metallurgical processes into a finite number of reaction zones. An 'Effective Reaction Zone (ERZ)' is a modeled volume comprising multiple phases and a reaction interface that is assumed to reach equilibrium.

To maintain the process continuum, adjacent reaction zones homogenize at another modeled frequency. Consequently, the kinetics of a process are simulated by modifying the effective reaction zone volumes and homogenization frequency. The accuracy of EERZ modeling relies on experimental/industrial process data, plant measurements/observations, and computational fluid dynamics/physical modeling of the process. In the present work, all reactions are considered isothermal/adiabatic, as the vacuum tank degassing process does not involve any active combustion reaction. The determination of the homogenization frequency, guided by the momentum or fluid dynamic aspects of adjacent zones, governs how often these zones equilibrate.

Figure 3 provides a schematic representation of a VTD segmented into its Effective Reaction Zones (ERZs), illustrating different reactions, including gas bubbles. The de-N reaction modes, as shown in Figure 3, are as follows:

1. Nitrogen and other gases dissolved in the liquid steel are absorbed by rising inert gas bubbles, such as Ar, introduced into the molten metal.

$$[N]_{bulk} + [N]_{bulk} + (Ar)_{bubble} \rightarrow (Ar + N_2)_{bubble} \quad (1)$$

2. Ar bubbles rise in the plume and become enriched with nitrogen and/or other dissolved gases.

$$[N]_{bulk} + [N]_{bulk} + (Ar + N_2)_{bubble} \rightarrow (Ar + 2\,N_2)_{bubble} \quad (2)$$

3. Spontaneous gas bubbles of nitrogen form at the ladle's eye, where the steel is directly exposed to the vacuum conditions under which the VTD is operating.

$$[N]_{bulk} + [N]_{bulk} \rightarrow (N_2)_{Vacuum} \quad (3)$$

4. Spontaneous nitrogen gas bubble formation in the bulk steel volume.

$$[N]_{bulk} + [N]_{bulk} \rightarrow (N_2)_{bubble} \quad (4)$$

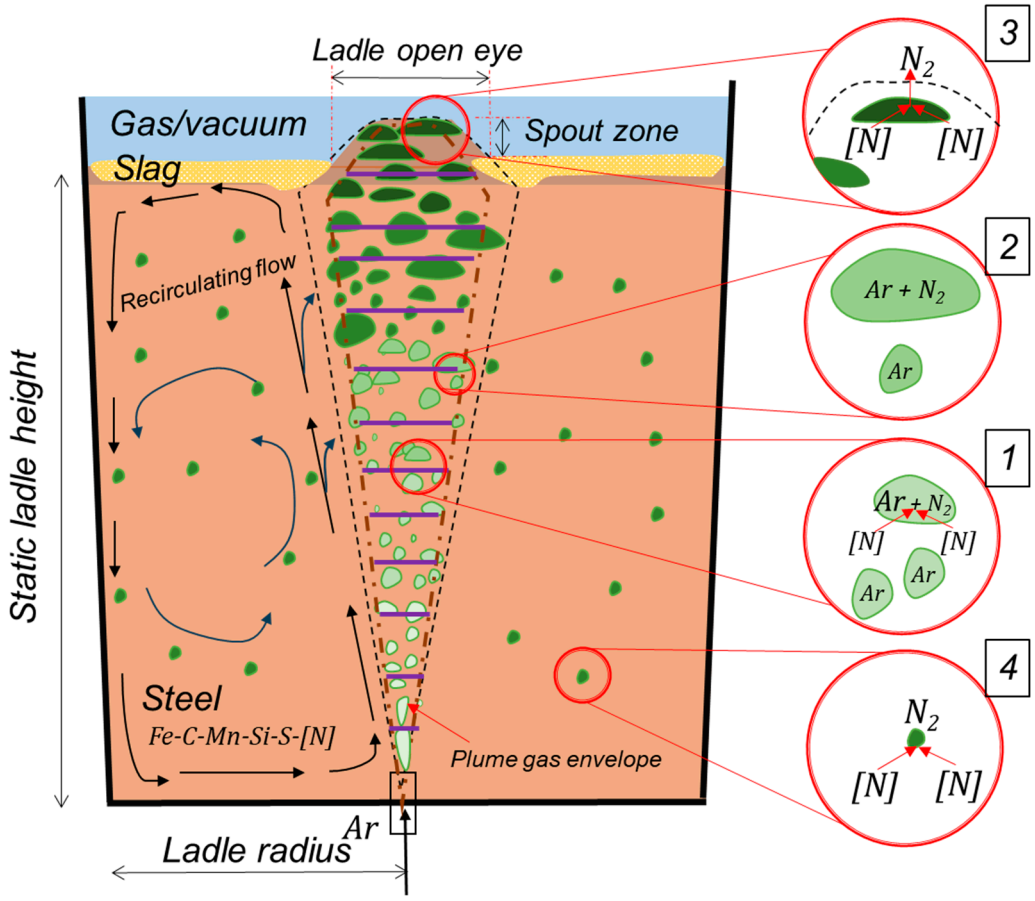

Figure 3. Schematic diagram of the VTD and the reaction zones included in the EERZ-based model. Black arrows indicate steel flow, while violet lines within the plume represent different reaction zones considered in the Z1 calculations. The dotted plume outlines volume changes at varying Ar injection rates. The four modes (1–4) of the de-N reaction are illustrated in the insets.

These modes will be referred to in Section 3.2 while explaining the VTD modeling flow sheet.

In the current VD simulation, three ERZs are considered, which are the following:

a. Zone at Eye (*Z_eye*): The volume of steel at the ladle eye (or spout region) that is exposed to the ambient atmosphere when the slag cover breaks due to the plume is classified as *Z_eye*. The ambient atmosphere is adjusted based on the vessel pressure data obtained from the VTD operation. In this study, the dimensionless eye (A_e/A_p) was calculated using relations derived by Krishnapisharody and Irons [29,30]:

$$\frac{A_e}{A_p} = \begin{cases} 0.91 - 0.12\chi^{-2}, \ \chi < 0.6 \\ 0.185 - 0.06\chi^{-2} + 2.535\chi, \ 0.6 \leq \chi < 0.75 \\ -0.54 + 5.07\chi, \ \chi \leq 0.75 \end{cases} \quad (5)$$

where χ is dependent on the slag (ρ_s) and steel (ρ_l) densities, Ar gas flow rate ($\dot{Q}_l$), standard condition gas flow rate ($\dot{Q}_N$), liquid steel height (H), and slag height (h_s). χ and the plume area [20] are calculated as

$$\chi = \left(1 - \frac{\rho_s}{\rho_l}\right)^{-0.5} \left(\frac{\dot{Q}_l}{g^{0.5}H^{2.5}}\right)^{0.32} \left(\frac{h_s}{H}\right)^{-0.5} \quad (6)$$

$$A_p = 1.41\left(Q^*\right)^{0.4} H^2 \quad (7)$$

Slag density was estimated to be approximately 2800 kg/m^3 (based on the respective slag chemistries), and slag height was measured to be 0.1 m (using pipe dips at the ladle station). During the process, Ar gas flow rate varies; therefore, a Microsoft Excel-based *Ladle Eye Solver* was developed using Equations (5)–(7) to calculate A_e/A_p and ladle eye size. Figure 4 illustrates the schematic representation of A_e/A_p and its variation as a function of the volumetric Ar flow rate as calculated by *Ladle Eye Solver*. Even though kinematic viscosity and the plume velocity have been reported [33] to influence A_e/A_p, it has not been considered in the current version of *Ladle Eye Solver*.

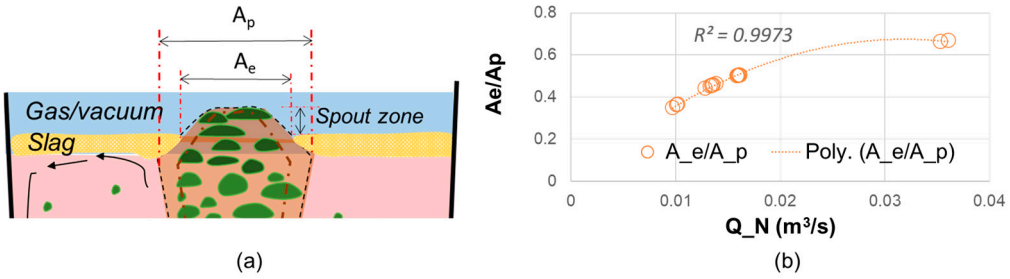

Figure 4. (**a**) Schematic representation of the plume area (A_p) and the ladle eye area (A_e). (**b**) Evolution of the dimensionless eye (A_e/A_p) with Ar flow rate.

Figure 5 shows a snapshot from the video recording of the ladle eye/spout zone during the degassing operation and the comparison between the measured and calculated ladle eye diameter over the processing time of 1000 s (~20 min). As can be seen in Figure 5b, ladle eye diameter measurements were reproduced by that calculated by *Ladle Eye Solver*. The differences between the calculation and measurements can be attributed to high temperature steel/slag/Ar fluid flow uncertainties and errors introduced in the measurements by exposure, strong bubbling, movement of the liquid steel and a one-dimensional observation of the spout.

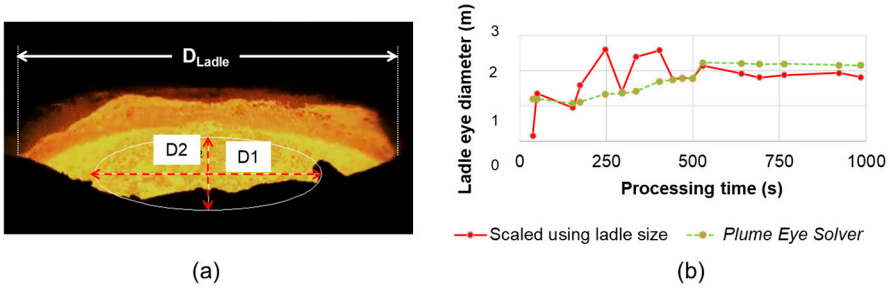

Figure 5. (**a**) The diameters D1 and D2 of the ladle eye area as obtained from the online video monitoring system. (**b**) Evolution of the ladle eye diameter as a function of processing time along with water modeling results [13,14].

b. Zone 1 (Z1)—Gas–Steel Interface: As shown in Figure 6, Z1 represents an interface zone between the gas bubbles and the steel in the plume (Zone 2 is explained in the following section). As illustrated in Figure 6a, de-N reaction is simulated by considering the amount of steel around the bubble, constituting Z1. The nitrogen in the plume (N_Z2) serves as a buffer, where the nitrogen in the Z1 steel (N_Z1) reacts (reaction: R1) with the Ar (and N_2) in the bubbles during active denitrogenation. To capture the evolution of gases and sizes of the bubbles, the Ar plume generated in the VTD is segmented into "*n*" sections (14 for the optimized EERZ presented here). Each respective section experiences different ferro-static pressure heads and flow conditions (Ar gas injection rate) during the VD process. The bubble size, therefore, changes depending on the local volumetric steel flow rate. Consequently, Z1 at a given

segment (Z1_n) and across the segments (Z1-1 to Z1-14) will evolve depending on the bubble diameter. The representative example of the bubble diameter variation along the VD processing in the respective segments is shown in Figure 6b. The derivation of the bubble diameter (d_B) is discussed below.

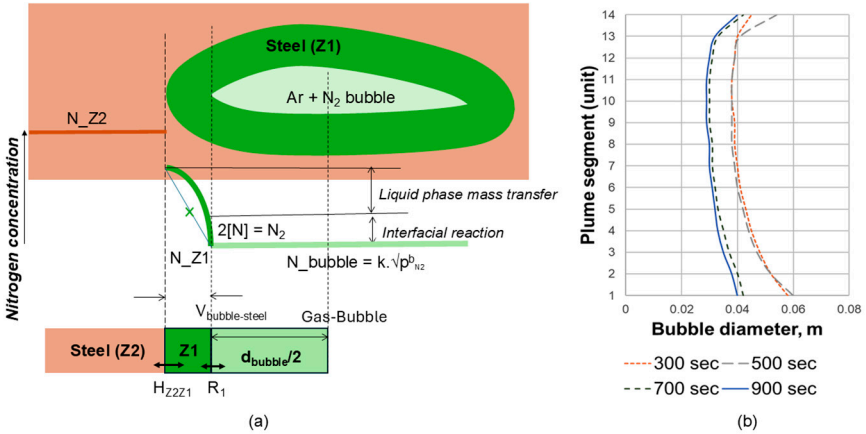

Figure 6. (**a**) Schematic representation of implementation of EERZ concept to model gas bubble/steel reaction along with the concentration profile of nitrogen inside the bubble, at Z1 and Z2. (**b**) Evolution of bubble diameter along the height of the plume (Ar plug to ladle eye).

The bubble size distribution in the plume is affected by the flow condition in the respective volume of the plume (Z1-1, Z1_2. . .Z1_n), bubble coalescence (due to collision), and breakup. The evolution of bubble sizes has been observed in several water modeling experiments [38–41]. From these water modeling experiments, it has been concluded that bubble breakup results from two opposing forces in the liquid steel: (a) turbulence, which promotes bubble distortion, and (b) surface tension, which restores the bubble shape. The frequency of bubble breakup (f_B) can then be attributed to the velocity of the disturbance (force imbalance) per the bubble perimeter (which is proportional to the bubble diameter) [42].

$$f_B = 0.25 \frac{\sqrt{8.2(\varepsilon d_B)^{2/3} - 12\sigma/(\rho_L d_B)}}{d_B} \tag{8}$$

where ε refers to the energy dissipation rate per unit mass of liquid steel, and σ and ρ_L refers to the surface tension and density of the liquid steel, respectively. In this study, the minimum diameter of the bubble (d_{min}) is calculated by $f_B = 0$ in Equation (8). Similarly, coalescence frequency is given as

$$f_C = 5.77\alpha^2\varepsilon^{1/3}{d_B}^{-11/3}\exp\left(-1.29\varepsilon^{1/3}{d_B}^{5/6}\sqrt{\rho_L/\sigma}\right) \tag{9}$$

where α is the volume fraction of bubbles. In Equation (9), the pre-exponential term represents the collision frequency, and the exponential term dictates the probability of coalescence. Both α and ε (fluid flow energy dissipation) will depend on Ar flow rate and the height in the plume (related actual pressure) during the degassing process and respective plume calculations

$$\alpha = 0.74{\dot{Q}_l}^{0.5}\bar{x}^{-1.25}(1-\xi)^{-1} \tag{10}$$

$$\varepsilon = \frac{\dot{n}_g RT}{\rho_l V_{p,total}} \ln \frac{H + h_a}{h_a} \tag{11}$$

ε is discussed in the following section on Zone 2 calculations. $\dot{Q}_l$ is the gas flow rate in the steel, which is different than $\dot{Q}_N$ (gas flow rate at standard temperature and pressure. $\dot{n}_g$ is the molar gas flow rate, and H and h_a are the liquid steel melt height and height at a given depth. A Microsoft-excel-based *bubble diameter* calculator was developed which dynamically calculates the α, ε, f_B, f_C and d_B, where ρ_L (7000 kg/m^3) and σ (1.8 N/m) are kept constant. The bubble diameter (d_B) is calculated by equating f_B and f_C, f_C can vary depending on the α and ε depending on the position inside the plume. The range of d_B calculated in this work (0.03–0.06 m) is comparable to that reported by Tang and Pistorius [42] and Bannenberg et al. [4]. As shown in Figure 6b, in this study, the evolution of the bubble diameter along the height of the plume is initially large (near the porous plug), decreases subsequently in the mid-height of the ladle (within the plume region), and then increases near the ladle eye. This trend is dissimilar to that discussed by Tang and Pistorius [42]. As the Z1 volume represents the envelope around the bubble, the thickness of this envelope is assumed to be a percentage (or fraction) of the bubble diameter. As discussed in a later section, this percentage was a modeling variable and was optimized to reproduce the observed de-N in the heats.

c. Zone 2 (Z2): The steel volume inside the plume region is calculated based on Ebneth and Pluschkell's expressions [43], which are incorporated to develop the Microsoft Excel-based *Plume volume solver*. The discussion and derivation of the expressions behind the solver were obtained from the references [43,44]. Figure 7a shows the schematic of the plume with the 14-Z1-segments. Figure 7b,c show the plume volume/shape as a function of Ar gas flow rate as calculated by the *Plume volume solver* and presented by Ebneth and Pluschkell [44] for 1 mbar and 1 atm atmospheric pressure, respectively. It should be noted that the plume size at the top part of the ladle, which is close to the ambient atmosphere, varies significantly with the vacuum condition. Such variations significantly influence the ladle eye size as shown in Figure 7b,c. The expansion in the plume size under vacuum conditions increases the surface nitrogen desorption due to enlarged bubble surface and plume eye area. This area, depending on slag characteristics (chemistry, temperature, etc.), can be correlated to ladle eye (*Z_eye*), contributing to maximum denitrogenation. For the present EERZ-based VTD model, the Z2 or plume volume is calculated by the process data of Ar gas flow rate and the pressure evolution along the VD processing time, utilizing the *Plume volume solver*. The VTD model allows spontaneous N_2 formation in Z2 (Figure 3: mode 4). It should be noted that the integration of *Ladle Eye Solver* and *Plume volume solver* is underway, considering the literature and available plant data.

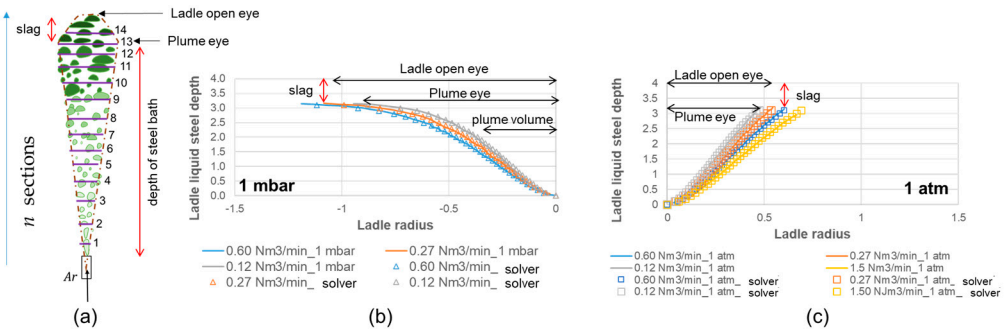

Figure 7. (**a**) Schematic diagram of Z2 with 14-Z1 segments. Variation in plume radius along the height of the plume at (**b**) 1 mbar and (**c**) 1 atm, along with data from reference [43,44].

d. Zone 3 (Z3): Steel outside the plume can be considered relatively stagnant, forming Z3 in the current modeling. Z3 is essentially the difference between the total steel volume

and the volumes of Zones 2 and 1. Like Z2, the VTD model allows spontaneous N_2 formation in Z3 (Figure 3: mode 4). Although slag properties have been considered to determine the *Z_eye* in this EERZ modeling work, steel-slag reactions will not be discussed.

3.2. EERZ Modeling Parameters, Tools, and Databases

The EERZ modeling primarily relied on the following inputs for respective heats:

a. Chemistry information:
   i. Steel: Fe-C-Mn-Si-Al-N-O-S
   ii. Slag: CaO-Al_2O_3-SiO_2-MgO-MnO-FeO
b. Mass information:
   i. Steel: 135 tons
   ii. Slag: 1–2 tons
c. Temperature: 1600 °C (isothermal condition)
d. Process conditions:
   i. Pressure of the ambient atmosphere
   ii. Ar gas flow rate
e. Solvers to determine ERZ volumes:
   i. *Ladle eye solver*
   ii. *Bubble diameter calculator*
   iii. *Plume volume solver*
f. Thermochemical modeling: FactSage version 8.3 [27] was used, with the following databases: FTmisc (for steel), FToxid (slag), and FactPS (gas).

The identification of the modeling parameters, tools, and databases was succeeded by the development of the modeling flow sheet that determined the time variable to predict reaction rates.

While the VTD model based on the EERZ approach can closely predict the actual N content (as shown in Figure 8), the calculation of a typical 13-min degassing process required approximately 24 h (i7–8 core processor with 16 GB-RAM). Consequently, there arose a need for a potential parametric correlation between the operational parameters determining Z1 and the de-N rate to facilitate quicker/online prediction of the N content.

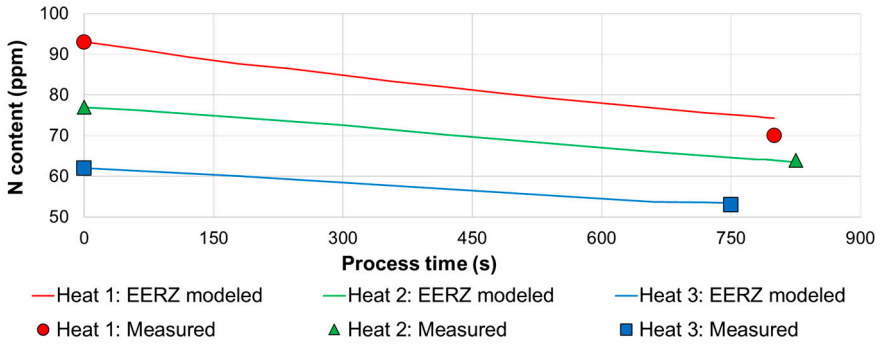

Figure 8. Comparison between the modeled and measured N content for three heats.

3.3. Methodology of VTD EERZ Model Execution

The methodology of EERZ-based VTD model implementation is listed below. The list captures the iterative model stages and the use of the underlying solvers used for the de-N simulation for the respective heats:

a. Initialization (t = 0)

i. Steel composition and temperature are initialized upon entry to the VTD station.
ii. Slag composition is incorporated to estimate the ladle eye size and zone volume (*Z_eye*).
iii. Process parameters: Argon injection, vessel pressure profiles, and total VD duration are model inputs.

b. First iteration (t = 1)
i. Zone calculations: The four reaction zones (*Z_eye*, Z1, Z2, and Z3) are computed using process inputs.
ii. *Z_eye* (ladle eye zone):
i. *Z_eye* area is determined using the *Plume Eye Solver.*
ii. *Z_eye* thickness is matched to the topmost Z1 segment (Z1_14).
iii. Steel mass within *Z_eye* reacts with ambient gases (or vacuum) using FactSage_Equilib module.
iii. Z1 (*Plume* zone- steel–bubble interaction):
i. Z1 volume varies with the process parameters along 14 (*n)* segments (Z1_1 to Z1_14) based on *bubble diameter calculations*.
ii. Each Z1 segment undergoes de-N reaction with gas bubbles using Modes 1 and 2 as shown in Figure 3.
iii. Inter-segment mixing and gas-steel mass updates are conducted for each time step.
iv. The N content of each Z1 segment evolves according to the equilibrium reaction in FactSage.
v. Evolved gases, especially from Z1_14, are recorded and exported to Excel
iv. Z2 (Plume adjacent steel volume).
i. Calculated using *Plume Volume Solver*
ii. Spontaneous N_2 formation is allowed as per Mode 4 in Figure 3.
iii. Periodic homogenization with Z1 and *Z_eye* occurs at a modeled time step (t_{12N}).
v. Z3 (Bulk steel volume):
i. This zone allows spontaneous N_2 formation (Mode 4).
ii. Homogenization with *Z_eye*, Z1, and Z2 occurs at a longer time interval (t_{123N}).
vi. All zone interactions and mixing processes are executed via FactSage-Equilib macro-coding.

c. Key model parameters for model calibration
i. The following modeling parameters were essential to improve the predictive accuracy of the final nitrogen content:
i. *Z_eye* thickness was calibrated to match the thickness of Z1_14 rather than a fixed value (like 0.1 m).
ii. Z1 volume was linked directly to predicted bubble diameters (D_b) across plume segments. Three cases were evaluated:
1. 4% D_b: overpredicted final nitrogen content.
2. 12% D_b: provided the best agreement with plant data.
3. 20% D_b: underpredicted final nitrogen content.
These results confirm that Z1 thickness as a proportion of bubble

diameter is an important model parameter and can change with steel/gas bubble chemistry.

iii. Homogenization frequencies:

1. t_{12N}: Z1-Z2 steel mixing.
2. t_{123N}: Z1-$_{Z2}$-Z3 steel homogenization.

4. Results

4.1. Modeling Results and Discussion: Steel Nitrogen Content Predictions (3 Heats)

The fixed set of modeling parameters was then applied to simulate the de-N process of Heats 1–3. A comparison of the measured and EERZ-model-simulated nitrogen contents is presented in Figure 8. The EERZ model slightly overcalculated the final nitrogen content for Heat 1 (74 ppm vs. measured 70 ppm) and provided precise estimations for Heats 2 (64 ppm) and 3 (53 ppm).

The over-estimation of final nitrogen for Heat 1 (~6% error), although minimal, can be attributed to zone-specific de-N mechanisms and assumptions of the EERZ model. As previously detailed, the removal of nitrogen from steel involves both the reaction of gas bubbles with the steel in the plume (Zone 1 or Z1) and the interaction of vacuum with the steel exposed at the ladle eye (*Z_eye*). Both mechanisms have been incorporated into the EERZ model, allowing for the quantification, comparison, and correlation of their contributions to de-N relative to the operational conditions of Heat 1's VD operations, such as modifications in Ar flow rate and vacuum conditions.

Figure 9 illustrates the impact of these two mechanisms in relation to VD operational conditions and the respective masses of Z1 and *Z_eye*. In Figure 9a, the *y*-axis provides an estimate of the nitrogen mass in the off-gas from the two sources during Heat 1's degassing. It reveals that the contribution of de-N from *Z_eye* is minimal until the vessel pressure drops to below ~10 torr, as depicted in Figure 9b, and gradually increases from approximately 7% to 22% with the onset of deep vacuum conditions. Therefore, in the later stages of degassing, out of the 2563 g of nitrogen removed from the steel (~135 t), almost 560 g was removed through the direct interaction of steel with vacuum at the ladle eye. These findings necessitate real-time or near-real-time tracking of *Z_eye* to improve de-N predictions and control, as explored in Section 4.6.

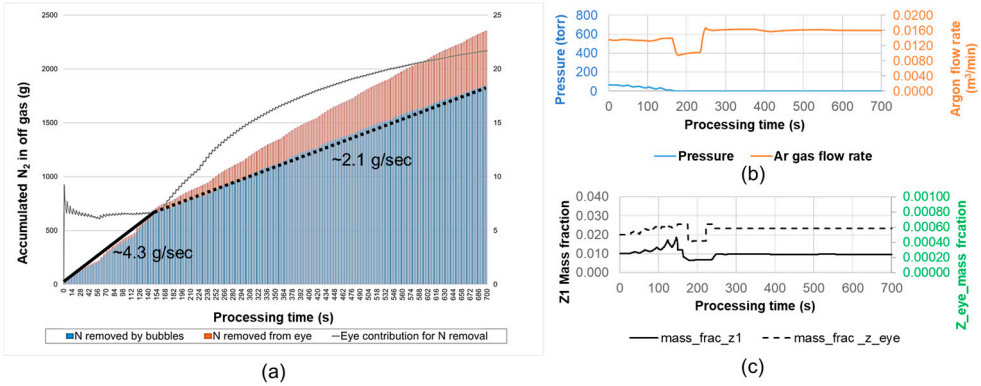

Figure 9. (**a**) Contribution of Z1 and *Z_eye* to the nitrogen removed during the complete processing time. The de-N rate (slope) has been superimposed. Variation in (**b**) process parameter (**c**) Z1 and *Z_eye* mass fractions with processing time.

In Figure 9a, the N-removal rate exhibits a drastic decrease at ~150 s from 4.3 g/s to 2.1 g/s, primarily due to the drop in N-removal by Z1 (steel–bubble reaction). This drop can be attributed to the decrease in the steel–bubble interaction volume (Z1 mass

fraction), as shown in Figure 9c, caused by bubble size reduction during the onset of deep vacuum conditions.

The current EERZ model also indicates that the most intense de-N from steel–bubble interaction (Z1 mass) occurs near the surface of the ladle eye, which can be tracked by plotting the Z1 fraction of sections n = 14, 7, and 1. The de-N process during the steel–bubble depends on the interaction volume of interacting steel surrounding the bubble: Z1.

In Figure 10, the graph depicts the Z1 volume change where a noticeable drop in the volume of steel–bubble interaction is observed around 150 s. Several instances from the Z1_volume change are illustrated by the green regions in inset sub-figures (a) to (d). As shown in inset illustrations (a)–(c), Z1, which has a thickness proportional to the average diameter of the bubbles, experiences an increase in volume as the pressure or Ar gas flow decreases. Under conditions that promote further bubble growth, the formation of closely packed bubbles reduces the volume of steel between them (Z2), which serves as a nitrogen reservoir.

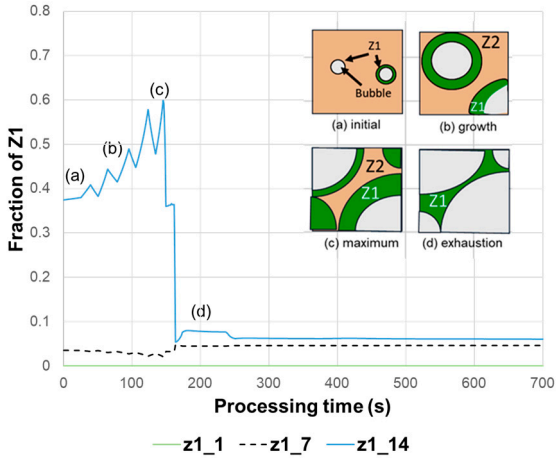

Figure 10. Evolution of the mass fraction of Z1 (steel–bubble interaction) at the top (14), middle (7), and bottom segment (1): 10 (**a**–**d**) shows the evolution of Z1 size and (**d**) exhaustion of steel due to bubble growth.

This exhaustion of steel volume between bubbles, as illustrated in Figure 10d, hinders reaction kinetics and retards de-N. Consequently, this decrease in steel volume leads to a reduction in the de-N rate, as shown in Figure 9. A similar phenomenon was reported in a study on MnO reduction by CO bubbles [45]. If this hypothesis holds true, it suggests the presence of an optimal range of Ar gas flow rates—sufficient to generate bubbles with an optimal size distribution for effective reaction with the steel, but not so high as to deplete the mass of steel between the bubbles, thereby reducing the nitrogen removal rate. A high vacuum remains desirable, and it primarily determines the final equilibrium nitrogen content.

4.2. Contribution of the EERZs to Denitrogenation in the VTD Model

Figure 11 illustrates the typical evolution of the four ERZs considered in the current VTD model alongside the change in nitrogen content (−ΔN content) in ppm. The ΔN content was determined by calculating the difference in average N content of the steel bath every 60 s of processing time through a homogenization reaction between the zones (*Z_eye*, Z1, Z2, and Z3). In Figure 11a, the mass fraction of Z1 gradually doubles, while that of *Z_eye*, Z2, and Z3 in Figure 11b–d marginally changed during the VD time. The evolution of Z1 (steel–bubble interaction volume) for the current heat is evident.

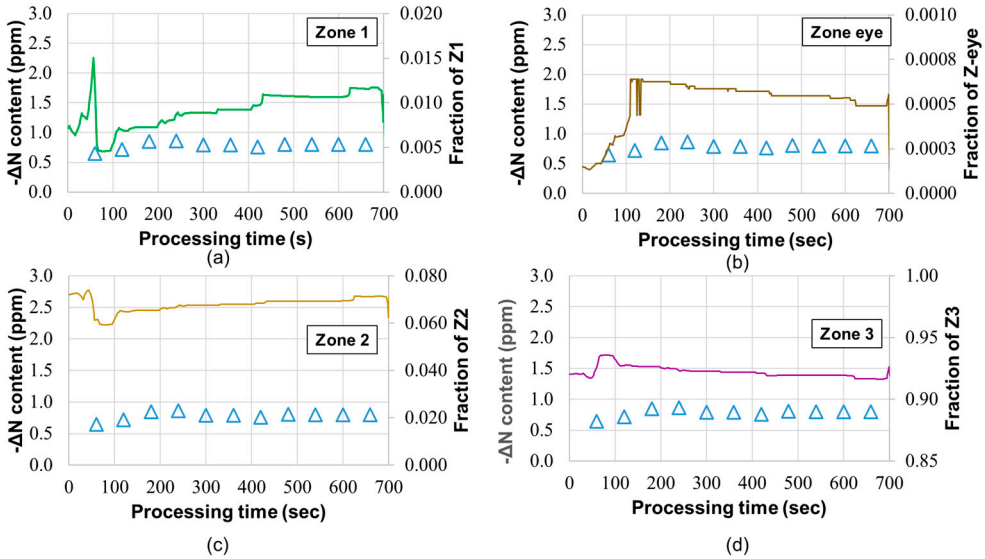

Figure 11. A typical evolution of change in the nitrogen content with the mass fraction of (**a**) Z1, (**b**) *Z_eye*, (**c**) Z2, and (**d**) Z3 as a function of processing time.

Similar correlations between -ΔN content and average Z1 fraction (every 60 s of processing time) were observed for all three heats, which are plotted in Figure 12.

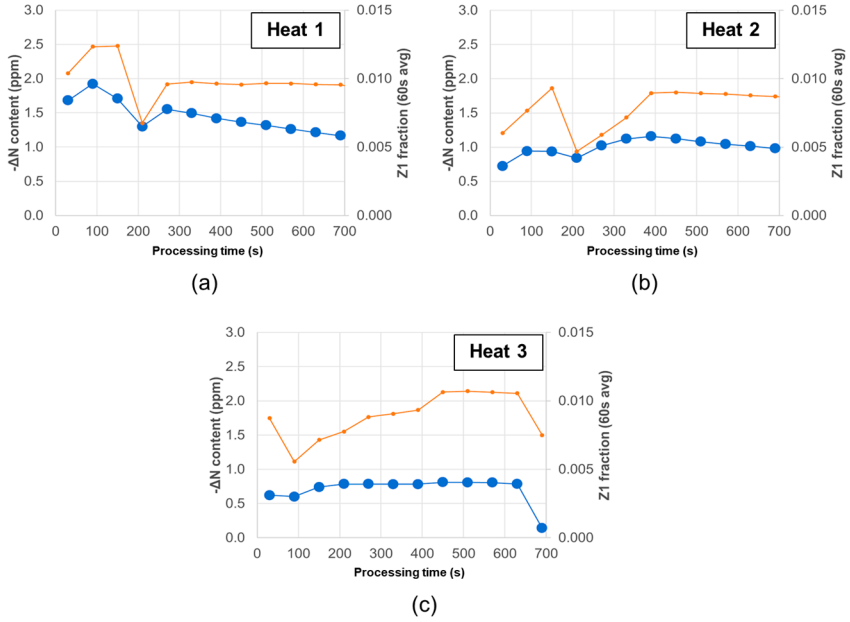

Figure 12. Evolution of average change in the nitrogen content and average Z1 mass fraction for (**a**) Heat 1, (**b**) Heat 2, and (**c**) Heat 3 as a function of processing time.

4.3. Simplification of the Model: ΔN Content vs. Average Z1 Correlation

Figure 13 illustrates the −ΔN content vs. the average Z1 fraction for all three heats modeled using the EERZ approach. In Figure 13a, a positive correlation is evident between the change in nitrogen content (−ΔN content) and the average Z1 fraction. The disparity in the slopes of the regression lines suggests differences in the de-N rates among the three heats shown in Figure 13a. These differences can be ascribed to variations in the driving force within the three heats, which, at any given time, is influenced by the difference between real-time and equilibrium N content. Anticipating minimal equilibrium N content due to the low pressure within the VTD, the driving force (directly proportional to the de-N rate) is primarily dependent on the real-time N content. The validation of this assumption

is depicted in Figure 13b, where the slope of the regression lines in Figure 13a (representing apparent average removal rates) shows a positive correlation with the initial N content (real-time N content).

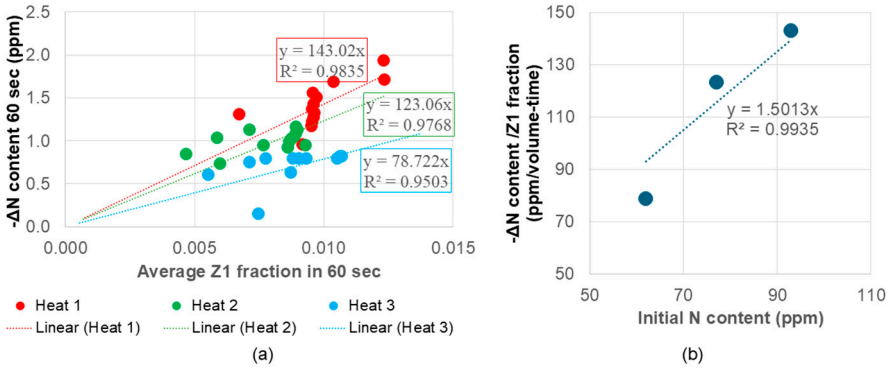

Figure 13. (**a**) Dependency of change in nitrogen content per 60 s on the average Z1 volume. (**b**) Correlation between de-N rate per unit average Z1 volume and the initial N content.

For steel grades of similar chemistries, a correlation between the ΔN content and Z1 has been established and extended to include the Ar injection pattern (Ar flow profile) and vacuum condition. The utilization of the parametric equation, instead of the EERZ-based VTD model, has significantly reduced prediction time and facilitated the exploration of avenues for improved VTD process efficiency and control. However, the EERZ-based model remains essential with changes in steel chemistries or process parameters such as temperature, slag depth/chemistry, etc.

4.4. Validation of the ΔN Content vs. Average-Z1 Correlation and Impact of Surface-Active Elements

The parametric equation has been applied to 22 heats from 12 different steel grades. In Figure 14a, a comparison between the modeled and measured $[N]_{final}$ (nitrogen content of steel after VD) is presented, with the dashed line representing an equivalent correlation and the green dashed line indicating deviation at a lower [N] ppm region. Generally, the modeled $[N]_{final}$ agrees with measured values; however, at concentrations below approximately 60 ppm, the model tends to overpredict. This deviation is attributed to differences in Z1 volumes among steel grades with varying chemistries. Previous studies [20,45–47] have also demonstrated that the de-N rate is significantly influenced by active sites (for absorption and desorption) for N at Z1, which are limited by the presence of surface-active elements such as S. The empirical model was developed using steel with a total sulfur [TS] after VTD in the range of 90–120 ppm [47].

For steel grades with lower TS, more active sites become available at the interface for the transport of nitrogen from the steel to the bubble. Consequently, the model underpredicts the de-N rate, resulting in a higher predicted $[N]_{final}$. The difference between the modeled and measured $[N]_{final}$ was plotted against the TS contents measured for the 22 heats, as shown in Figure 14b. The decreasing trend suggests that the empirical model will overpredict de-N for lower sulfur content, with the best agreement at TS = 100 ppm, which was the median value of the three heats originally used to develop the EERZ model-based correlation. The R^2 of the fitting is 0.5480, which can be attributed to the variety of vacuum pressures and Ar injection profiles adopted by operators based on incoming steel chemistry differences and process delays.

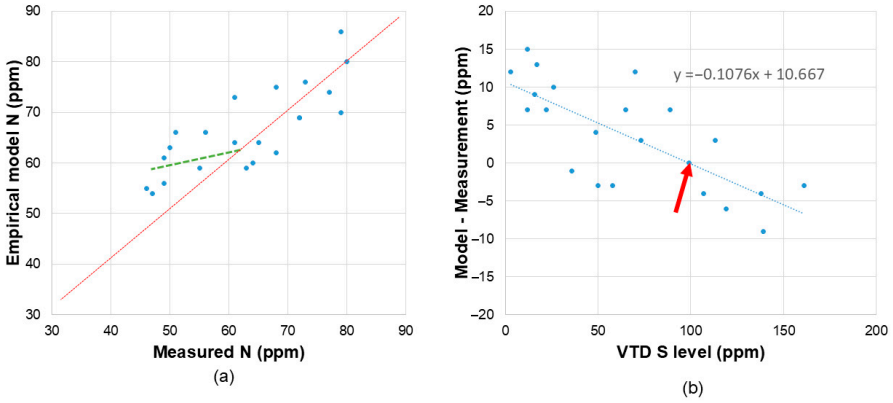

Figure 14. (**a**) Comparison of measured and calculated N content. (**b**) Correlation between VTD sulfur level and the difference between modeled and measured nitrogen content. N.B. The correlation fits best around TS 100 ppm and can be updated with a pool of data.

Previous studies [3,20,46] have shown that the nitrogen removal rate constant (k''_N) decreases with increasing activities of dissolved oxygen and sulfur, with oxygen having a more pronounced inhibitory effect. This trend aligns with our observations, where the EERZ model tended to underpredict de-N for heats with lower total sulfur content.

Based on this observation, the empirical correlation was corrected, leading to a significant improvement in predictions, especially for low nitrogen heats, where 17 out of 22 heats had an error of ±7 ppm, and 21 out of 22 within ±10 ppm. Although steel chemistries vary in C, Mn, and Si (Table 1), their effects on Z1 were not investigated for further refinement of the empirical correlations.

4.5. Contribution of the Z_eye to Denitrogenation in the VTD Model

While the refined empirical model improves predictions by accounting for surface-active elements influencing Z1, nitrogen removal during VTD is also significantly impacted by transient flow behavior and physical exposure of molten steel to vacuum. In particular, the contribution of the ladle eye (*Z_eye*) becomes critical under deep vacuum conditions. This section explores the dynamic role of *Z_eye* using high-temperature video recordings and EERZ model predictions.

Z_eye (Zone at Eye) refers to the molten steel surface exposed when the slag cover breaks due to Ar bubble buoyancy, creating a direct path for nitrogen removal under vacuum. At ladle stations, operators use high-temperature video recordings to monitor ladle eye opening and shape evolution—key indicators of plug performance in both hard and soft stirring. For consistency, videos from heats of a specific steel grade were analyzed using a Python 3.10 with Spyder IDE 5.4.3 based algorithm that automates video processing by extracting frames, thresholding RGB and grayscale channels, and calculating cumulative exposure areas (CEA). The green channel offered the clearest representation with minimal noise. High-exposure contours from each channel were overlaid, and the combined data was used to generate output videos and tabulated frame-wise *Exposure metric*. Figure 15 shows a representative frame and processed contours, which were benchmarked against *Z_eye* predictions from the EERZ model to validate visual observations.

When the exposure metric correlated with the injected Ar gas volume, as shown in Figure 16a, the unprocessed data appeared skewed in the high gas injection volume region. Upon further analysis, as in Figure 16b, a direct correlation between the exposure metric and the injected gas volume was observed. This qualitatively validates the direct relationship between ladle eye behavior and the volume of gas injected. The exposure metric was calculated every 0.25 s and averaged over each second, which also enabled estimation of the associated error due to variability. At lower gas injection rates, the exposure metric is

primarily influenced by the presence of steel droplets and mostly includes data from the last minute of injection.

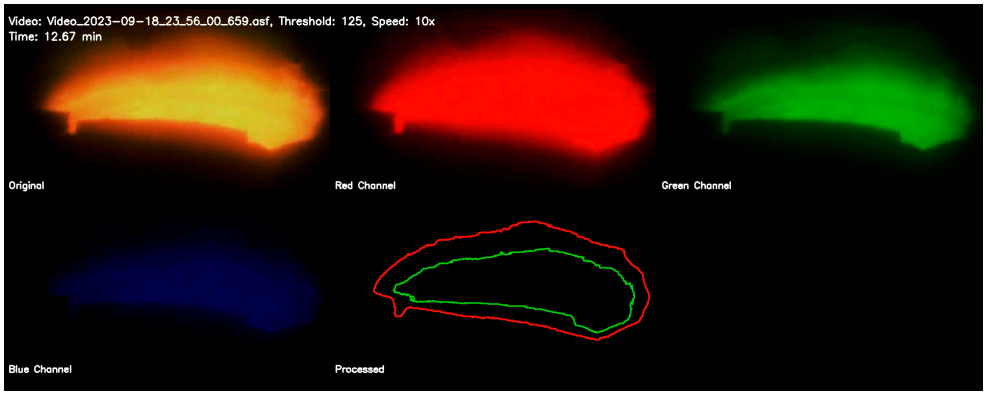

Figure 15. Screenshot from the output video feed with Original, Red, Green, and Blue Channel and Processed contours.

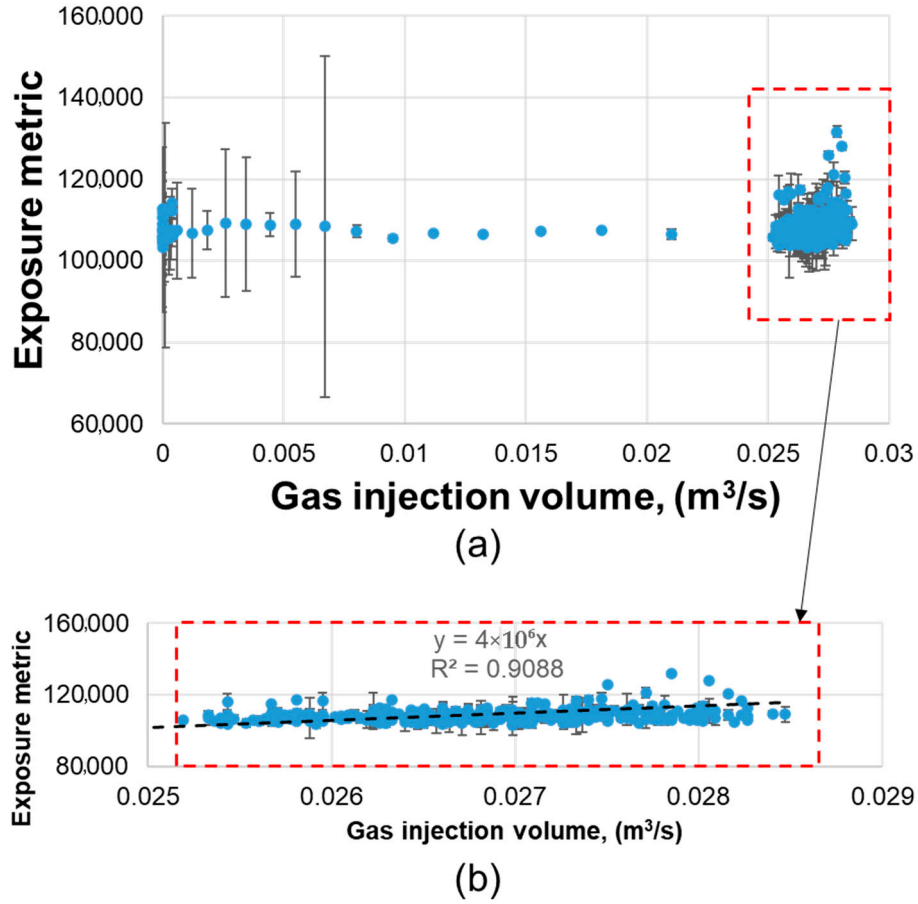

Figure 16. (**a**) Raw exposure metric data vs. Ar gas volume, showing high-volume skewness. (**b**) Close-up during degas-stirring revealing a clear correlation.

As shown in Figure 17, (a) the operational parameters, namely vacuum pressure and gas flow rate affect the (b) exposure metric variation, which directly correlates with (c) gas flow rate. An increase in Ar flow causes more frequent bubble rupture, enlarging the exposed eye and thereby increasing the *Exposure metric*. Notably, the observed drop in the *Exposure metric* can be correlated with the operating condition, primarily Ar gas flow rate through the ladle plug at the lowest vacuum pressure. This also informed the truncation of

Figure 17a down to Figure 17c which can be further used to investigate denitrogenation response under lowest vacuum pressures.

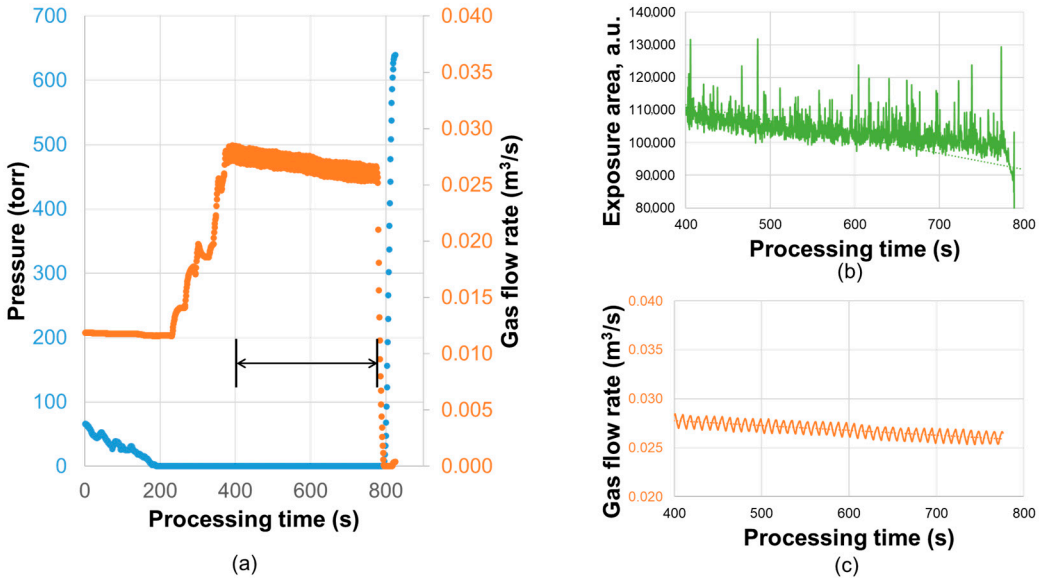

Figure 17. (**a**) Variation in operational parameters: pressure and gas flow rate over time. (**b**) Exposure metric response and (**c**) gas flow rate during processing time.

It is worthwhile examining the simulated contribution of EERZ-predicted *Z_eye* and the video-derived exposure metric (cumulative exposure areas: CEA) to nitrogen removal as a function of operational parameters at the VTD. Both the exposure metric and *Z_eye* become particularly significant when the vessel pressure drops below 10 torr.

The *Z_eye* observed from plant data, acting as a time-dependent contributor to de-N—especially under deep vacuum conditions—has been used to validate the *Z_eye* predicted by the EERZ model. Simulation results suggest that *Z_eye* plays a minimal role in nitrogen removal at pressures above 10 torr, mainly due to the lack of sufficient driving force for surface reactions. However, once the vessel reaches deep vacuum conditions (<10 torr), *Z_eye* becomes increasingly important.

As shown in Figure 17, during the deep vacuum period (400–750 s), the CEA estimates indicate a gradual decrease in *Z_eye*'s contribution, which can be directly linked to a reduction in Ar gas injection flow rate.

A qualitative correlation was observed between the video-derived CEA and the model-predicted *Z_eye* volumes in Figure 18. Increased Ar flow introduces more Ar bubbles that frequently rupture at the slag/steel interface. This rupture disrupts the slag layer, forming the eye and expanding the exposed steel surface area, thereby elevating CEAs. To further characterize this behavior, a *stirring (intensity) metric* is introduced, derived from vibration data obtained using a sensor mounted on the degasser shell. This metric captures the forces generated by gas injection, bubble formation (including spontaneous formation from vacuum-exposed surfaces), bubble coalescence and breakup, slag displacement, slag/steel shearing, and refractory interactions. These stirring effects initially fluctuate but stabilize as the Ar flow and the vacuum condition become steady. As steady-state conditions are reached, both *Z_eye* exposure and the de-N rate also stabilize. This dynamic response highlights the EERZ model's effectiveness in capturing transient multiphase phenomena during vacuum degassing.

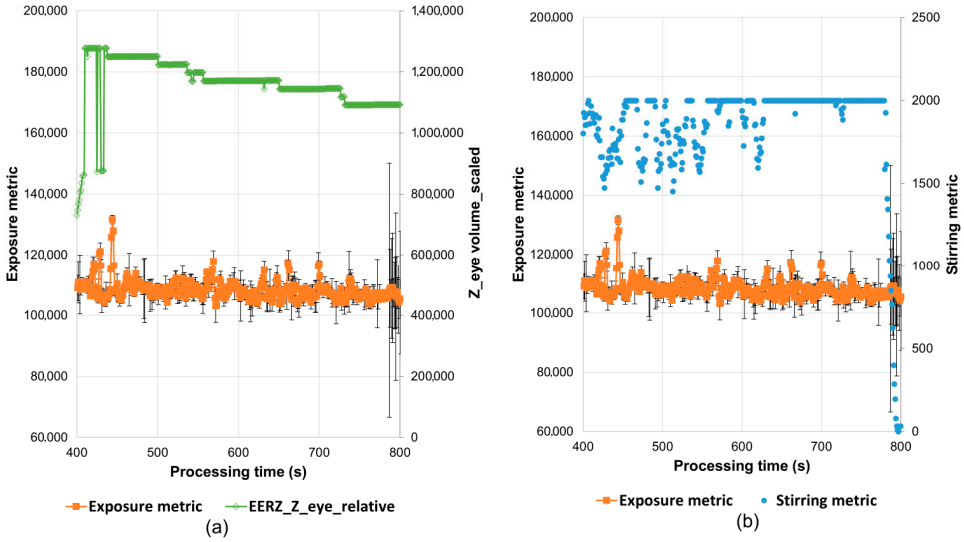

Figure 18. (**a**) Exposure metric (CEA) from RGB channels and modeled *Z_eye* volume (scaled). (**b**) Exposure metric and stirring intensity metric as a function of processing time.

The integration of visual data and *stirring metric*, as shown in Figure 18b, with model predictions *Z_eye* (Figure 18a) enhances the robustness of the VTD simulation framework. This enables comprehensive parametric analysis and multi-heat tracking of de-N performance.

Building upon the insights from *Z_eye* behavior and model validation, further improvements to the EERZ model will be carried out to enhance accuracy and scope.

4.6. Discussion and Future Work

Zone 3 (Z3) in the EERZ model—representing the nitrogen reserve—is currently oversimplified, ignoring concentration gradients from mass transfer variations. Refining Z3 via segmentation based on velocity or momentum could improve accuracy, albeit at the cost of increased simulation time.

Degassing effects on the plume are evaluated using the Ar injection rate and pressure to estimate bubble and plume sizes. As de-N progresses, increasing gas content enlarges the bubbles. Since zone volume depends on interfacial area, the current Z1 and Z2 estimates may be conservative. CFD simulations of bubble-induced steel flow could help address these limitations.

Intense stirring can break slag and introduce droplets into the steel. While the EERZ model is being updated for desulfurization predictions, capturing slag droplet and slag-bubble interaction effects requires better insight into high-temperature slag-gas dynamics, which are still poorly understood. Enhanced image acquisition, acoustic and/or vibration data acquisition from plant operations, combined with advanced image processing, may help bridge this gap. The *stirring metric* presented in this study, derived from vibration sensor data, will be further extended to account for more erratic vacuum and argon gas injection profiles. Together with the *exposure metric*, this metric can serve as a valuable diagnostic tool to flag degassing anomalies and improve real-time monitoring and control during VTD operations.

Off-gas analysis of the VTD exhaust and validation with the EERZ model will be of great importance, especially when the oxygen content of the steel or the slag FeO-content are high, which can cause foaming. Additionally, non-isothermal EERZ simulations will be necessary to model later ladle operations like arcing and alloying. It should also be noted that the isothermal assumption in the VD model may be a potential source of error, as a temperature loss of approximately 3 °C/min is observed under vacuum conditions.

5. Summary and Key Takeaways

This study developed and validated an EERZ modeling framework to simulate nitrogen removal during Vacuum Degassing. Key process parameters such as steel and slag chemistry, steel and slag mass, vacuum pressure, and argon injection profiles were integrated with thermochemical databases (FactSage 8.3) and physical model-based solvers to predict nitrogen content across multiple heats. The schematic in Figure 19 outlines the core modeling tools, methodology, predicted values, metrics (exposure and stirring), and validation outputs and correlations.

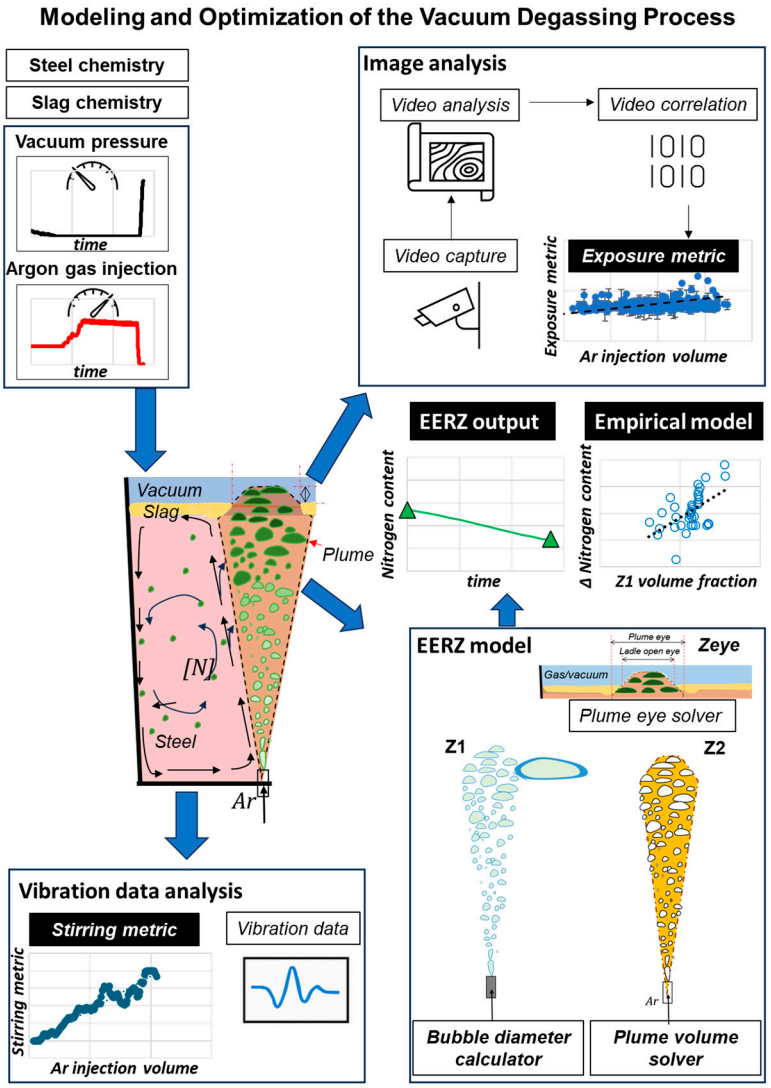

Figure 19. Schematic of the model implementation with highlights of the key process parameters, methodology, and sub-models (solvers and calculators) used to simulate and optimize the vacuum degassing process.

Although slag viscosity was nearly constant, variations in slag thickness and density were analyzed using dynamics and ladle eye (*Z_eye*) zones. The EERZ model effectively captured the dynamic contributions of steel–bubble (Z1) and steel–vacuum (*Z_eye*) interfaces to nitrogen removal, particularly under deep vacuum (<10 torr). A strong correlation was established between nitrogen reduction (ΔN) and volume Z1, enabling simplified real-time predictions. Additionally, the influence of surface-active elements such as sulfur on nitrogen removal via the Z1_volume was evident.

This work also explores the correlation of *Z_eye* behavior of EAF-sourced heats with high-temperature video data obtained from a single-plug VTD process. The video-derived CEA and *Z_eye* values under low vacuum conditions were found to be a function of argon injection volume, with accompanying vibration intensity data presented. A stirring intensity metric, derived from vibration data, was introduced to complement visual (and video-derived CEA) observations and detect process anomalies related to gas injection, bubble dynamics, and slag/steel interactions.

Overall, the model establishes a robust foundation for operational optimization and offers potential for future extensions to incorporate desulfurization and non-isothermal effects.

6. Conclusions

The following key conclusions summarize the outcomes and implications of this study based on the validated EERZ modeling framework and supporting plant data:

- Primary Vacuum Degassing (VD) parameters were reviewed, and a kinetic VTD model was developed using the EERZ framework.
- The EERZ framework of the VTD model incorporates operational data such as vacuum pressure, argon injection profiles, and steel and slag chemistries to determine zones Z1, Z2, Z3, and *Z_eye* throughout the VD heat.
- The VTD model simplified nitrogen removal by focusing on four zones (Z1, Z2, Z3, and *Z_eye*), with the plume (Z1) divided into 14 vertical segments to track pressure and bubble evolution.
- Steel–bubble interaction (Z1) was confirmed as the dominant mechanism for nitrogen removal under vacuum.
- The model was validated using operational data and end-point chemistry from three production heats.
- A parametric correlation between nitrogen removal and Z1 volume reduced simulation time from ~24 h to under 1 min, offering a practical route for online predictions.
- The correlation's accuracy improved by accounting for surface-active elements, particularly sulfur, which affects reaction site availability.
- Slag composition and thickness were integrated into the ladle eye (*Z_eye*) prediction using physical correlations and image processing tools.
- High-temperature video analysis confirmed the role of *Z_eye* in de-N under deep vacuum (<10 torr), validating EERZ-predicted exposure behavior.
- Incorporating visual metrics (CEA) into the modeling framework enhanced robustness and supported real-time tracking of ladle eye dynamics.
- The EERZ model effectively captures thermo-kinetics and multiphase interactions in VTD and can be further refined using CFD, extended plant datasets, and non-isothermal simulations.

Author Contributions: Conceptualization, B.K. and N.Q.; methodology, B.K.; software, B.K.; validation, N.Q., B.K. and M.S.; formal analysis, B.K.; investigation, N.Q.; resources, N.Q., B.K. and M.S.; data curation, N.Q. and B.K.; writing—original draft preparation, B.K.; writing—review and editing, M.S.; visualization, B.K.; supervision, B.K.; project administration, B.K. All authors have read and agreed to the published version of the manuscript.

Funding: This research received no external funding.

Data Availability Statement: The data presented in this study are available on reasonable request from the corresponding author. Restrictions apply due to the inclusion of proprietary, confidential, or third-party information, and to ensure compliance with privacy and data protection standards.

Acknowledgments: The authors would like to acknowledge the technical contributions of A. Hamilton and M. Richards (EVRAZ NA R&D) and the trial support provided by R. Zeien (EVRAZ NA Pueblo Steel). The contributions of Keyan Miao and Ziyi Wang (former employees at EVRAZ NA R&D) in preparing the initial versions of the equilibrium and EERZ model and analyzing trial data are also gratefully recognized. Appreciation is also extended to the Degasser station team at EVRAZ NA Pueblo Steel for their operational assistance. The authors further acknowledge valuable discussions with Sheldon Swick (EVRAZ NA Regina Steel) during image processing. This article is a revised and expanded version of a paper entitled "Study of the Vacuum Degassing Process Using the Effective Equilibrium Reaction Zone Model", which was presented at AISTech 2024—Proceedings of the Iron & Steel Technology Conference, 6–9 May 2024, Columbus, Ohio, USA.

Conflicts of Interest: Authors Bikram Konar, Noah Quintana, and Mukesh Sharma are employees of EVRAZ North America. All the authors declare that the research was conducted in the absence of any commercial or financial relationships that could be construed as a potential conflict of interest.

Abbreviations

The following abbreviations are used in this manuscript:

CEA	Cumulative Exposure Areas
Z_eye	Ladle Eye Region
VD	Vacuum Degassing
EERZ	Effective Equilibrium Reaction Zone
EAF	Electric Arc Furnace
de-N	Denitrogenation
dmin	Minimum Diameter of the Bubble
ERZ	Effective Reaction Zone
XRF	X-Ray Fluorescence
OES	Optical Emission Spectrometer
LRV	Ladle Resonance Value

References

1. Yu, S.; Miettinen, J.; Louhenkilpi, S. Modeling Study of Nitrogen Removal from the Vacuum Tank Degasser. *Steel Res. Int.* **2014**, *85*, 1393–1402. [CrossRef]
2. Yu, S.; Miettinen, J.; Louhenkilpi, S. Mathematical Modeling of Nitrogen Removal from the Vacuum Tank Degasser. *Steel Res. Int.* **2015**, *86*, 467–477. [CrossRef]
3. Thoms, S.; Tu, S.; Janke, D. Denitrogenation of Steel Melts with Oxygen and Sulphur by Injection of Argon under Reduced Pressure. *Steel Res.* **1997**, *68*, 475–478. [CrossRef]
4. Bannenberg, N.; Bergmann, B.; Gaye, H. Combined Decrease of Sulphur, Nitrogen, Hydrogen and Total Oxygen in Only One Secondary Steelmaking Operation. *Steel Res.* **1992**, *63*, 431–437. [CrossRef]
5. Lichterbeck, R.; Laraudogoitia, J.; Kleimt, B.; Köhle, S.; Stender-Robertz, J.; Ors, F. *Dynamic Modelling and Control of the Vacuum Degassing Process: Secondary Steelmaking: Final Report*; Publications Office of the European Union: Luxembourg, 2001.
6. He, S.; Zhang, G.; Wang, Q. Desulfurization Process in RH Degasser for Soft-Killed Ultra-Low-Carbon Electrical Steels. *ISIJ Int.* **2012**, *52*, 977–983. [CrossRef]
7. Li, M.; Yang, Y.; Shao, L.; Zhou, Z. A Numerical Study on Dehydrogenation of Liquid Steel Supersaturated with Hydrogen in a Vacuum Degasser (VD). *Metall. Mater. Trans. B* **2023**, *54*, 681–693. [CrossRef]
8. Charlotte, M. Influence of Stirring on the Inclusion Characteristics During Vacuum Degassing in a Ladle. Master's Thesis, KTH Royal Institute of Technology, Stockholm, Sweden, 2015.
9. Malmberg, K.; Nzotta, M.; Karasev, A.; Jonsson, P.G. Optimization of Stirring Conditions during Vacuum Degassing in Order to Lower Inclusion Content in Tool Steel. *Ironmak. Steelmak.* **2013**, *40*, 231–237. [CrossRef]
10. Mintz, B. Influence of Nitrogen on Hot Ductility and Transverse Cracking in Steels. *ISIJ Int.* **1999**, *39*, 833–855. [CrossRef]
11. Shen, Y.; Hansen, S.S. Effect of the Ti/N Ratio on the Hardenability and Mechanical Properties of a Quenched-and-Tempered C-Mn-B Steel. *Metall. Mater. Trans. A* **1997**, *28*, 2027–2035. [CrossRef]
12. Berns, H.; Kleff, J.; Krauss, G.; Foley, R.P. Microstructure and Tensile Behavior of Nitrogen-Alloyed, Dual-Phase Stainless Steels. *Metall. Mater. Trans. A* **1996**, *27*, 1845–1859. [CrossRef]

13. Kitamura, T.; Miyamoto, K.; Tsujino, R.; Mizoguchi, S.; Kato, K. Mathematical Model for Nitrogen Desorption and Decarburization Reaction in Vacuum Degasser. *ISIJ Int.* **1996**, *36*, 395–401. [CrossRef]
14. Rigas, K.; Willers, B.; Eckert, S.; Glaser, B. Investigations on Vibrational Interpretations of Bubbles in Metal-Making Processes. *Metall. Mater. Trans. B* **2023**, *54*, 2105–2120. [CrossRef]
15. Kostetskyi, Y.; Kukuy, D.; Kvasov, I.; Khodyachikh, V.; Degtyarenko, I.; Omelchenko, A. Application of vibroacoustic monitoring technique on a ladle furnace unit during steel treatment. In Proceedings of the Metal 2007 International Metallurgical & Materials Conference, Hradec nad Moravicí, Czech Republic, 22–24 May 2007.
16. Rigas, K.; Willers, B.; Eckert, S.; Glaser, B. Vibrations Analysis of Bubble Evolution in Liquids of Varying Physical Properties. *Metall. Mater. Trans. B* **2024**, *55*, 229–241. [CrossRef]
17. Pylvänäinen, M.; Visuri, V.; Nissilä, J.; Laurila, J.; Karioja, K.; Ollila, S.; Fabritius, T.; Liedes, T. Vibration-Based Monitoring of Gas-Stirring Intensity in Vacuum Tank Degassing. *Steel Res. Int.* **2020**, *91*, 1900587–1900597. [CrossRef]
18. Pylvänäinen, M.; Visuri, V.; Liedes, T.; Laurila, J.; Karioja, K.; Pikkupeura, S.; Ollila, S.; Fabritius, T. Vibration-based Assessment of Gas Stirring Intensity in Ladle Treatments. In Proceedings of the 5th International Conference on Process Development in Iron and Steelmaking, Luleå, Sweden, 12–15 June 2016.
19. Yenus, J.; Brooks, G.; Dunn, M.; Li, Z.; Goodwin, T. Study of Low Flow Rate Ladle Bottom Gas Stirring Using Triaxial Vibration Signals. *Metall. Mater. Trans. B* **2018**, *49*, 423–433. [CrossRef]
20. Fruehan, R.J.; Martonik, L.J. The Rate of Absorption of Nitrogen into Liquid Iron Containing Oxygen and Sulfur. *Metall. Mater. Trans. B* **1980**, *11*, 615–621. [CrossRef]
21. Ban-Ya, S.; Ishii, F.; Iguchi, Y.; Usui, T. Rate of Nitrogen Desorption from Liquid Iron–Carbon and Iron–Chromium Alloys with Argon. *Metall. Mater. Trans. B* **1988**, *19*, 233–242. [CrossRef]
22. Ono-Nakazato, H.; Dohi, Y.; Yamada, D.; Usui, T. Effects of Cu, Sn and W on the rate of nitrogen dissociation on the surface of molten iron. *ISIJ Int.* **2006**, *46*, 1306–1311. [CrossRef]
23. Choh, T.; Yamada, T.; Inouye, M. Rates of Nitrogen Absorption into Liquid Fe–Cr and Fe–Cr–Ni Alloys. *Tetsu-to-Hagane* **1976**, *62*, 334–343. [CrossRef]
24. Harashima, K.; Mizoguchi, S.; Matsuo, M.; Kiyose, A. Rates of Nitrogen and Carbon Removal from Liquid Iron in Low Content Region under Reduced Pressures. *ISIJ Int.* **1992**, *32*, 111–119. [CrossRef]
25. Harashima, K.; Mizoguchi, S.; Kajioka, H.; Sakakura, K. Kinetics of Nitrogen Desorption from Liquid Iron with Low Nitrogen Content under Reduced Pressures. *Tetsu-to-Hagane* **1987**, *73*, 1559–1566. [CrossRef]
26. Yu, S.; Louhenkilpi, S. Numerical Simulation of Dehydrogenation of Liquid Steel in the Vacuum Tank Degasser. *Metall. Mater. Trans. B* **2013**, *44*, 459–468. [CrossRef]
27. Jung, I.-H.; Van Ende, M.-A. Computational Thermodynamic Calculations: FactSage from CALPHAD Thermodynamic Database to Virtual Process Simulation. *Metall. Mater. Trans. B* **2020**, *51*, 1851–1874. [CrossRef]
28. Van Ende, M.-A.; Jung, I.-H. A Kinetic Ladle Furnace Process Simulation Model: Effective Equilibrium Reaction Zone Model Using FactSage Macro Processing. *Metall. Mater. Trans. B* **2017**, *48*, 28–36. [CrossRef]
29. Krishnapisharody, K.; Irons, G. A Model for Slag Eyes in Steel Refining Ladles Covered with Thick Slag. *Metall. Mater. Trans. B* **2015**, *46*, 191–198. [CrossRef]
30. Krishnapisharody, K.; Irons, G. Modeling of Slag Eye Formation over a Metal Bath Due to Gas Bubbling. *Metall. Mater. Trans. B* **2006**, *37*, 763–772. [CrossRef]
31. Iguchi, M.; Miyamoto, K.; Yamashita, S.; Iguchi, D.; Zeze, M. Spout Eye Area in Ladle Refining Process. *ISIJ Int.* **2004**, *44*, 636–638. [CrossRef]
32. Amaro-Villeda, A.M.; Ramirez-Argaez, M.A.; Conejo, A.N. Modeling of Fluid Flow and Inclusion Removal in a Tundish under Electromagnetic Stirring. *ISIJ Int.* **2014**, *54*, 1–8. [CrossRef]
33. Peranandhanthan, M.; Mazumdar, D. Numerical Simulation of Melt Flow and Inclusion Behavior in Tundish under Different Pouring Conditions. *ISIJ Int.* **2010**, *50*, 1622–1631. [CrossRef]
34. Wu, L.; Valentin, P.; Sichen, D. Physical and Mathematical Modelling of Melt Flow in a Gas-Stirred Ladle. *Steel Res. Int.* **2010**, *81*, 508–515. [CrossRef]
35. Ramasetti, E.K.; Visuri, V.; Sulasalmi, P.; Palovaara, T.; Gupta, A.K.; Fabritius, T. Physical and CFD Modeling of the Effect of Top Layer Properties on the Formation of Open-Eye in Gas-Stirred Ladles with Single and Dual-Plugs. *Steel Res. Int.* **2019**, *90*, 1900088. [CrossRef]
36. Conejo, A.N.; Feng, W. Mathematical Modeling of Turbulent Flow and Mixing in a Slab Caster Tundish. *Metall. Mater. Trans. B* **2022**, *53*, 999–1017. [CrossRef]
37. Bale, C.W.; Bélisle, E.; Chartrand, P.; Decterov, S.A.; Eriksson, G.; Gheribi, A.E.; Hack, K.; Jung, I.-H.; Kang, Y.-B.; Melançon, J.; et al. FactSage Thermochemical Software and Databases, 2010–2016. *Calphad* **2016**, *54*, 33–53. [CrossRef]
38. Zhou, M.; Brimacombe, J.K. Critical Fluid Flow Phenomenon in a Gas-Stirred Ladle. *Metall. Mater. Trans. B* **1994**, *25*, 681–693. [CrossRef]

39. Anagbo, P.E.; Brimacombe, J.K. Plume Characteristics and Liquid Circulation in Gas Injection through a Porous Plug. *Metall. Mater. Trans. B* **1990**, *21*, 637–648. [CrossRef]
40. Alexiadis, A.; Gardin, P.; Domgin, J.F. Spot Turbulence, Breakup, and Coalescence of Bubbles Released from a Porous Plug Injector into a Gas-Stirred Ladle. *Metall. Mater. Trans. B* **2004**, *35*, 949–956. [CrossRef]
41. Pistorius, P.C. *Bubbles in Process Metallurgy*; Elsevier Ltd.: Oxford, UK, 2013; Volume 2.
42. Tang, D.; Pistorius, P.C. Kinetics of Nitrogen Removal from Liquid Third Generation Advanced High-Strength Steel by Tank Degassing. *Metall. Mater. Trans. B* **2022**, *53*, 1383–1395. [CrossRef]
43. Ebneth, G.; Pluschkell, W. Dimensional Analysis of the Vertical Heterogeneous Buoyant Plume. *Steel Res.* **1985**, *56*, 513–518. [CrossRef]
44. Jamieson, B.J.; Tabatabaei, Y.; Barati, M.; Coley, K.S. Kinetics of the Carbothermic Reduction of Manganese Oxide from Slag. *Metall. Mater. Trans. B* **2019**, *50*, 192–203. [CrossRef]
45. Fruehan, R.J.; Goldstein, D.; Sarma, B.; Story, S.R.; Glaws, P.C.; Pasewicz, H.U. Recent Advances in the Fundamentals of the Kinetics of Steelmaking Reactions. *Metall. Mater. Trans. B* **2000**, *31*, 891–898. [CrossRef]
46. Inomoto, T.; Kitamura, S.; Yano, M. Kinetic Study of the Nitrogen Removal Rate from Molten Steel (Normal Steel and 17 mass% Cr Steel) under CO Boiling or Argon Gas Injection. *ISIJ Int.* **2015**, *55*, 1822–1827. [CrossRef]
47. Konar, B.; Miao, K.; Quintana, N.; Wang, Z. Study of the Vacuum Degassing Process Using the Effective Equilibrium Reaction Zone Model. In Proceedings of the Iron & Steel Technology Conference AISTech 2024, Columbus, OH, USA, 6–9 May 2024; pp. 731–745.